

Topological edge state coupled mode-induced tetra-band tunable spin-dependent perfect absorption

Ji-Peng Wu(伍计鹏), Xi-Rui Zeng(曾玺瑞), Yu-Lei Liao(廖煜磊), Rong-Zhou Zeng(曾荣周), Hong Wen(文鸿), Xiao-Yu Dai(戴小玉), and Yuan-Jiang Xiang(项元江)

Citation: Chin. Phys. B, 2026, 35 (**4**): 047801. DOI: 10.1088/1674-1056/ae00b2
http://cpb.iphy.ac.cn; http://iopscience.iop.org/cpb

What follows is a list of articles you may be interested in

Investigation of reflection anisotropy induced by micropipe defects on the surface of a 4H-SiC single crystal using scanning anisotropy microscopy

Wei Huang(黄威), Jinling Yu(俞金玲), Yu Liu(刘雨), Yan Peng(彭燕),Lijun Wang(王利军), Ping Liang(梁平), Tangsheng Chen(陈堂胜), Xiangang Xu(徐现刚), Fengqi Liu(刘峰奇), and Yonghai Chen(陈涌海)
Chin. Phys. B, 2024, 33 (**3**): 037801. DOI: 10.1088/1674-1056/acf27f

Effect of thickness of antimony selenide film on its photoelectric properties and microstructure

Xin-Li Liu(刘欣丽), Yue-Fei Weng(翁月飞), Ning Mao(毛宁), Pei-Qing Zhang(张培晴), Chang-Gui Lin(林常规), Xiang Shen(沈祥), Shi-Xun Dai(戴世勋), and Bao-An Song(宋宝安)
Chin. Phys. B, 2023, 32 (**2**): 027802. DOI: 10.1088/1674-1056/ac8724

Dual-channel tunable near-infrared absorption enhancement with graphene induced by coupled modes of topological interface states

Zeng-Ping Su(苏增平), Tong-Tong Wei(魏彤彤), and Yue-Ke Wang(王跃科)
Chin. Phys. B, 2022, 31 (**8**): 087804. DOI: 10.1088/1674-1056/ac6744

A flexible ultra-broadband metamaterial absorber working on whole K-bands with polarization-insensitive and wide-angle stability

Tao Wang(汪涛), He-He He(何贺贺), Meng-Di Ding(丁梦迪), Jian-Bo Mao(毛剑波), Ren Sun(孙韧), and Lei Sheng(盛磊)
Chin. Phys. B, 2022, 31 (**3**): 037804. DOI: 10.1088/1674-1056/ac306e

Effects of substitution of group-V atoms for carbon or silicon atoms on optical properties of silicon carbide nanotubes

Ying-Ying Yang(杨莹莹), Pei Gong(龚裴), Wan-Duo Ma(马婉铎), Rui Hao(郝锐), and Xiao-Yong Fang(房晓勇)
Chin. Phys. B, 2021, 30 (**6**): 067803. DOI: 10.1088/1674-1056/abdb1e

---

Topological edge state coupled mode-induced tetra-band tunable spin-dependent perfect absorption

Ji-Peng Wu(伍计鹏)[1], Xi-Rui Zeng(曾玺瑞)[1], Yu-Lei Liao(廖煜磊)[1], Rong-Zhou Zeng(曾荣周)[1], Hong Wen(文鸿)[2], Xiao-Yu Dai(戴小玉)[3], and Yuan-Jiang Xiang(项元江)[3,†]

[1] *School of Transportation and Electrical Engineering, Hunan University of Technology, Zhuzhou* 412007, *China*
[2] *School of Aerospace, Hunan University of Technology, Zhuzhou* 412007, *China*
[3] *College of Electrical and Electronic Engineering, Wenzhou University, Wenzhou* 325935, *China*

(Received 24 July 2025; revised manuscript received 18 August 2025; accepted manuscript online 29 August 2025)

When discussing the spin-dependent optical perfect absorption (PA) phenomenon in a micro-nano structure, the designed structure should contain symmetry-breaking compositions that generally require an applied magnetic field. Fortunately, the multi-Weyl semimetal (mWSM) with natural time-reversal symmetry breaking property provides feasible schemes to investigate the spin-dependent PA without an external magnetic field. Recently, most existing schemes are primarily restricted to single- or dual-band spin-dependent PA in mWSM-based systems. Here, we present a heterostructure comprising five one-dimensional photonic crystals (PCs) and four identical mWSM layers to discuss the tetra-band spin-dependent PA. Results show that, due to the topological edge state-coupled mode and the nonzero off-diagonal term of mWSM, the PA of left-hand circularly polarized and right-hand circularly polarized light is attained at four distinct frequencies, respectively. More importantly, the tetra-band spin-dependent PA phenomenon can be regulated effectively via the tilt degree of Weyl cones, Fermi energy, topological charge, Weyl nodes separation, mWSM thickness, and the periods of the middle three PCs. This study provides an efficient scheme to achieve tetra-band adjustable spin-dependent PA without an external magnetic field, which may have potential applications in spin-dependent photonic devices.

Keywords: perfect absorption, multi-Weyl semimetal, photonic crystals, topological edge state

PACS: 78.20.Ci, 78.40.–q, 78.20.Ls, 78.67.Pt

DOI: 10.1088/1674-1056/ae00b2 **CSTR:** 32038.14.CPB.ae00b2

1. Introduction

Recently, optical absorbers have attracted broad attention due to their practical applications in solar photovoltaic cells and numerous optoelectronic fields.[1,2] A variety of schemes and compositions have been proposed to achieve optical perfect absorption (PA), such as epsilon-near-zero materials,[3] graphene-hexagonal boron nitride hyper-crystals,[4] and surface plasmon resonance,[5] among others. In particular, one-dimensional (1D) photonic crystals (PCs), which are manufacturable 1D microstructures with cyclical spatial modulation in refractive index, can generate photonic bandgaps to prevent light propagation.[6–8] Exploiting photonic bandgaps enables feasible schemes to achieve PA, such as critical coupling,[9] optical Tamm states,[10] and related methods. However, these schemes generally focus on linear-polarization PA.

Spin-dependent optical absorption, a particular optical absorption phenomenon, arises from distinct absorption behaviors of right-hand circular polarization (RCP) and left-hand circular polarization (LCP).[11] Circular polarization, carrying spin angular momentum, shows unique advantages due to its specific interaction with chiral materials, its ability to carry quantum information, its stability during propagation, and its rich physical effects. These features make it a key research focus in fields such as biology, quantum technology, communication, and imaging.[12–14] Investigating spin-dependent optical absorption in micro-nano structures usually requires symmetry-breaking chiral compositions, often achieved with an external magnetic field.[15] However, the large size of magnetic systems limits experimental investigation and potential applications. Therefore, developing chiral materials that function without applied magnetic fields is of great significance for studying spin-dependent PA.

Weyl semimetals (WSMs) have recently attracted growing attention due to their prominent optical properties, such as graphene-like tunable plasmons and excellent optical nonlinearity.[16,17] The Weyl nodes in a WSM act as sources or sinks of Berry curvature, effectively serving as a magnetic field in momentum space.[18] WSMs arise when either spatial inversion or time-reversal symmetry is broken. In WSMs with broken time-reversal symmetry (TRS), chiral features persist even without an external magnetic field. Typically, conventional WSMs carry topological charge $n = 1$, as identified in NbAs, TaP, and TaAs.[19–21] Recently, higher topological charges of 2 and 3 have been discovered.[22] WSMs with enhanced topological charge are called multi-WSMs (mWSMs), found in $SrSi_2$, $HgCr_2Se_4$, $TI(MoTe)_3$, and $Rb(MoTe)_3$.[23–25] Generally, mWSMs exhibit optical performances similar to conventional WSMs.[22]

†Corresponding author. E-mail: xiangyuanjiang@126.com

© 2026 Chinese Physical Society and IOP Publishing Ltd. All rights, including for text and data mining, AI training, and similar technologies, are reserved.

The chiral features of WSM and mWSM have been widely studied, including applications in circular polarizers,[26] Kerr and Faraday effects,[27,28] optical isolators,[29] and circularly polarized thermal radiation.[30] Recently, a Fabry–Pérot cavity with mWSM was proposed to discuss spin-dependent PA,[31] and a conventional Otto configuration with WSM was presented by Ma *et al.*[32] to achieve spin-dependent PA. However, most existing schemes are limited to single- or dual-band spin-dependent PA. Multi-band spin-dependent PA remains largely unexplored. Compared with single- or dual-band PA, multi-band spin-dependent PA can accommodate complex multi-band signals, enhance information processing capabilities, and broaden application scenarios such as multispectral imaging and multi-channel communication.[33,34] Therefore, developing mWSM-based systems to achieve multi-band spin-dependent PA is of great significance.

Topological edge states (TES) have recently gained attention for their topological protection and enhanced local-field features.[35–37] Various designs have been developed to generate photonic TES modes.[38,39] In particular, the simple and manufacturable nature of 1D PCs allows the excitation of TES modes for studying optical phenomena such as optical bistability,[40] optical group delay,[41] and thermal radiation.[42] TES modes emerge in 1D PCs when two contiguous PCs possess opposite topological characteristics within overlapping bandgaps. Excitation of TES modes leads to narrow frequency peaks within the TES bandgap.[43] Hence, exploiting TES modes in 1D PC heterostructures provides a feasible scheme to realize optical PA.

In this work, we propose a heterostructure comprising five PCs and four identical mWSM layers to achieve tetra-band spin-dependent PA by combining TES-coupled modes with the chiral properties of mWSMs. By tuning the tilt of Weyl cones, Fermi energy, topological charge, Weyl nodes separation, mWSM thickness, and periods of the middle three PCs, the four PA frequencies for LCP and RCP can be flexibly controlled. This study provides an effective scheme to achieve tetra-band adjustable spin-dependent PA without an external magnetic field and may hold potential for tunable multi-band spin-dependent photonics, including multispectral imaging and multi-channel communication.

2. Model and theoretical method

To realize tetra-band spin-dependent PA, we design a heterostructure comprising five 1D PCs and four identical mWSM layers, as illustrated in Fig. 1. PC1, PC3, and PC5 consist of the unit cell ABA with periods N_1, N_3, and N_5, respectively, while PC2 and PC4 consist of the unit cell BAB with periods N_2 and N_4. The thicknesses of constituents A and B in the unit cells ABA and BAB are d_1, d_2, d_3, and d_4, respectively. Materials A and B are Si and SiO_2, with refractive indices $n_A = 3.48$ and $n_B = 1.45$ in the operating frequency range. The thicknesses d_1, d_2, d_3, and d_4 are chosen as 0.27Λ, 0.46Λ, 0.36Λ, and 0.32Λ, respectively, where $\Lambda = \lambda_0/(4n_A) + \lambda_0/(4n_B)$ and $\lambda_0 = 4$ μm is the central wavelength. The C layer represents the mWSM layer with thickness $d_m = 1.36$ μm, and the D layer is a PEC substrate to block light transmission.

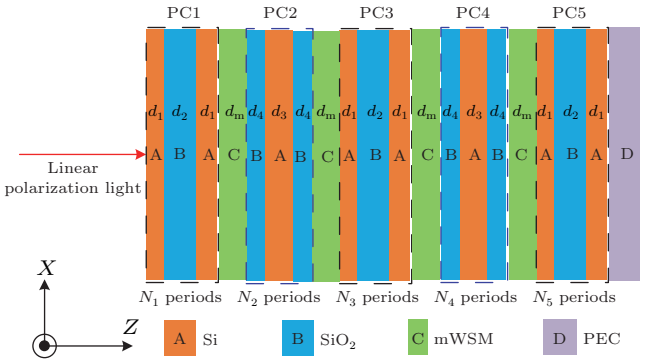


Fig. 1. Schematic diagram of the proposed heterostructure for tetra-band spin-dependent PA. The structure consists of five 1D photonic crystals (PCs) and four identical mWSM layers. PC1, PC3, and PC5 comprise the unit cell ABA with periods N_1, N_3, and N_5, respectively, while PC2 and PC4 comprise the unit cell BAB with periods N_2 and N_4, respectively. The thicknesses of components A and B in the unit cells ABA and BAB are d_1, d_2, d_3, and d_4, respectively. The mWSM layers have thickness d_m, with the two discrete multi-Weyl nodes oriented along the z-axis.

Considering the TRS-broken mWSM containing two separate multi-Weyl nodes along the z direction, its conductivity is described by a 3×3 tensor[22]

$$\overline{\overline{\sigma}} = \begin{pmatrix} \sigma_{xx} & \sigma_{xy} & 0 \\ \sigma_{yx} & \sigma_{yy} & 0 \\ 0 & 0 & \sigma_{zz} \end{pmatrix}, \tag{1}$$

where $\sigma_{xx} = \sigma_{yy}$ denote the longitudinal conductivities, $\sigma_{xy} = -\sigma_{yx}$ the Hall conductivities, and σ_{zz} the longitudinal conductivity along z, which does not affect the Fresnel reflection under normal incidence.

Using the Kubo formula with conduction and valence band wave functions, the longitudinal and Hall conductivities of type-I mWSMs with $C = C_+ = -C_- < 1$ are obtained, where C_χ is the tilt degree of the Weyl cones and $\chi = \pm 1$ denotes the opposite chirality of the pair of Weyl nodes. Explicitly, these conductivities are written as[22]

$$\mathrm{Re}(\sigma_{xx}) = \begin{cases} 0, & \omega < \omega_1, \\ \sigma_\omega^n \left(\frac{1}{2} - \kappa_d\right), & \omega_1 < \omega < \omega_2, \\ \sigma_\omega^n, & \omega > \omega_2, \end{cases} \tag{2}$$

$$\begin{aligned} \mathrm{Im}(\sigma_{xx}) = -\frac{\sigma_\omega^n}{4\pi} \Bigg[& \xi \ln \frac{|\omega_2^2 - \omega^2|}{|\omega_1^2 - \omega^2|} + \frac{8}{|C|^2} \left(\frac{\mu}{\hbar\omega}\right)^2 \\ & - \left(\frac{\mu}{\hbar\omega}\right)^3 \zeta(\omega, |C|, \mu) \ln \frac{|\omega_2 - \omega|(\omega_1 + \omega)}{|\omega_1 - \omega|(\omega_2 + \omega)} \\ & + \frac{6}{|C|^3} \left(\frac{\mu}{\hbar\omega}\right)^2 \ln \frac{|\omega_2^2 - \omega^2|\omega_1^2}{|\omega_1^2 - \omega^2|\omega_2^2} + 4 \ln \frac{|\omega_c^2 - \omega^2|}{|\omega_2^2 - \omega^2|} \Bigg], \end{aligned} \tag{3}$$

$$\mathrm{Re}(\sigma_{xy}^{\mathrm{ac}}) = \mathrm{sgn}(C)\, \sigma_\mu^n \left[-\frac{1}{2|C|^2} \ln \frac{|\omega_2^2 - \omega^2|\omega_1^2}{|\omega_1^2 - \omega^2|\omega_2^2} \right.$$

$$+\left(\frac{\mu}{2\hbar\omega|C|^2}+\frac{\hbar\omega}{8\mu}\frac{1-|C|^2}{|C|^2}\right)\ln\frac{|\omega_2-\omega|(\omega_1+\omega)}{|\omega_1-\omega|(\omega_2+\omega)}-\frac{1}{|C|}\Bigg], \tag{4}$$

$$\mathrm{Re}(\sigma_{xy}^{\mathrm{dc}})=\sigma_Q^n+\sigma_\mu^n\left(\frac{2}{C}+\frac{1}{C^2}\ln\frac{1-C}{1+C}\right), \tag{5}$$

$$\mathrm{Re}(\sigma_{xy})=\mathrm{Re}(\sigma_{xy}^{\mathrm{ac}})+\mathrm{Re}(\sigma_{xy}^{\mathrm{dc}}), \tag{6}$$

$$\mathrm{Im}(\sigma_{xy})=\mathrm{sgn}(C)\begin{cases}0, & \omega<\omega_1,\\ 3\sigma_\omega^n\kappa_{\mathrm{o}}, & \omega_1<\omega<\omega_2,\\ 0, & \omega>\omega_2,\end{cases} \tag{7}$$

where the symbols are defined as

$$\sigma_\omega^n=\frac{e^2n\omega}{6h\nu_{\mathrm{F}}},\quad \sigma_Q^n=\frac{e^2nQ}{\pi h},\quad \sigma_\mu^n=\frac{e^2\mu n}{h^2\nu_{\mathrm{F}}},$$
$$\kappa_{\mathrm{o}}=\frac{1}{|C|^2}\left(\frac{1}{8}-\frac{\mu}{2\hbar\omega}+\frac{\mu^2}{2\hbar^2\omega^2}\right)-\frac{1}{8},$$
$$\zeta(\omega,|C|,\mu)=\frac{4}{|C|^3}+3\left(\frac{\hbar\omega}{\mu}\right)^2\left(\frac{1}{|C|^3}+\frac{1}{|C|}\right),$$
$$\kappa_{\mathrm{d}}=\left(\frac{2\mu}{\hbar\omega}-1\right)\left[\frac{3}{8|C|}+\frac{1}{8|C|^3}\left(\frac{2\mu}{\hbar\omega}-1\right)^2\right],$$
$$\xi=2+\frac{1}{2|C|^3}+\frac{3}{2|C|},\quad h=2\pi\hbar,\quad \omega_{\mathrm{c}}=k_{\mathrm{c}}\nu_{\mathrm{F}}.$$

The relevant dielectric tensor of the mWSM is then

$$\varepsilon_{xx}=\varepsilon_b+\frac{\mathrm{i}\sigma_{xx}}{\omega\varepsilon_0},\quad \varepsilon_{xy}=\frac{\mathrm{i}}{\omega\varepsilon_0}(\sigma_{xy}+\sigma_Q^n). \tag{8}$$

To evaluate optical absorption, the Fresnel reflection coefficients are computed via a 4×4 anisotropic transfer matrix to account for the off-diagonal term $\gamma=\varepsilon_{xy}/\mathrm{i}$. For our structure with a PEC substrate, the absorption of LCP and RCP light is

$$A_-=1-R_-,\quad A_+=1-R_+.$$

The four degenerate TES modes in the PC/mWSM heterostructure split into four linear-polarization absorption peaks, and the nonzero γ allows realization of tetra-band PA for LCP and RCP light.

3. Results and discussions

To investigate the excitation of TES modes in a heterostructure composed of two 1D PCs, the band structures of the individual PCs are first analyzed using the dispersion relation[43,44]

$$\cos(KL)=\cos(k_{\mathrm{A}}d_{\mathrm{A}})\cos(k_{\mathrm{B}}d_{\mathrm{B}})+\left(\frac{Z_{\mathrm{A}}}{Z_{\mathrm{B}}}+\frac{Z_{\mathrm{B}}}{Z_{\mathrm{A}}}\right)\sin(k_{\mathrm{A}}d_{\mathrm{A}})\sin(k_{\mathrm{B}}d_{\mathrm{B}}), \tag{9}$$

where L is the unit cell width, K the Bloch wavevector, k_i the wave vector along the z direction, d_i the total thickness of medium i, and $Z_i=\sqrt{\mu_i/\varepsilon_i}$ is the impedance of medium i with permeability μ_i and permittivity ε_i ($i=$ A or B).

The Zak phase of the mth isolated passband between the mth and $(m-1)$th bandgaps, θ_m^{Zak}, is calculated by[43,44]

$$\exp(\mathrm{i}\theta_m^{\mathrm{Zak}})=-\frac{\mathrm{sgn}(\varphi_{m-1})}{\mathrm{sgn}(\varphi_m)}, \tag{10}$$

where φ_m and φ_{m-1} are the reflection phases of the mth and $(m-1)$th bandgaps, respectively. The sign function is defined as $\mathrm{sgn}(\varphi_m)=-1$ for $\varphi_m\in(-\pi,0)$ and 1 for $\varphi_m\in(0,\pi)$.

For the lowest 0th isolated band, the Zak phase simplifies to[43,44]

$$\exp(\mathrm{i}\theta_0^{\mathrm{Zak}})=\mathrm{sgn}\left(1-\frac{\varepsilon_{\mathrm{A}}\mu_{\mathrm{B}}}{\varepsilon_{\mathrm{B}}\mu_{\mathrm{A}}}\right). \tag{11}$$

Finally, the topological property of the qth bandgap is identified using[43,44]

$$\mathrm{sgn}[\varsigma^{(q)}]=(-1)^q(-1)^l\exp\left(\mathrm{i}\sum_{m=0}^{q-1}\theta_m^{\mathrm{Zak}}\right), \tag{12}$$

where l is the number of band crossings below the qth bandgap. A positive sign of $\varsigma^{(q)}$ indicates a positive topological feature, whereas a negative sign indicates a negative topological feature. The TES mode can be excited when the overlapping bandgaps of the two PCs exist and their topological signs are opposite.

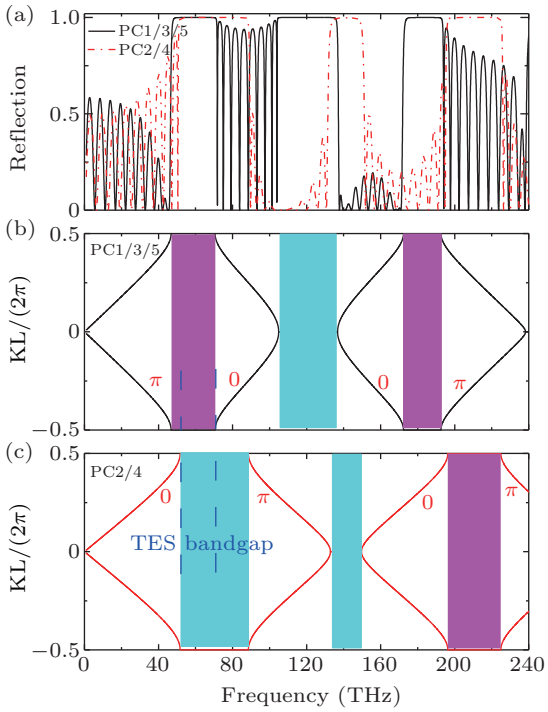


Fig. 2. TES bandgaps in the designed heterostructure with two 1D PCs. (a) Reflection spectra of PC1/3/5 and PC2/4. (b) and (c) Corresponding band structures of PC1/3/5 and PC2/4, respectively. Magenta rectangles indicate bandgaps with positive topological features, while cyan rectangles indicate bandgaps with negative topological features. The Zak phase of 0 or π is labeled in red within the pass bands.

To further demonstrate the feasibility of the TES mode in the designed heterostructure comprising two 1D PCs, Figs. 2(a)–2(c) show the reflection spectra of PC1/3/5 and

PC2/4, the band structures of PC1/3/5, and the band structures of PC2/4, respectively. Here, all five PCs are chosen to have identical periods of 10.

As seen in Fig. 2(a), three bandgaps appear in the reflection spectra of both PC1/3/5 and PC2/4, with the first and second bandgaps partially overlapping. The band structures shown in Figs. 2(b) and 2(c) are in good agreement with these reflection characteristics. Notably, while there are two overlapping bandgap regions between PC1/3/5 and PC2/4, only the first overlapping region exhibits opposite topological features. Therefore, the TES mode is expected to appear solely within this first overlapping bandgap, corresponding to the frequency range from 51.7 THz to 70.6 THz.

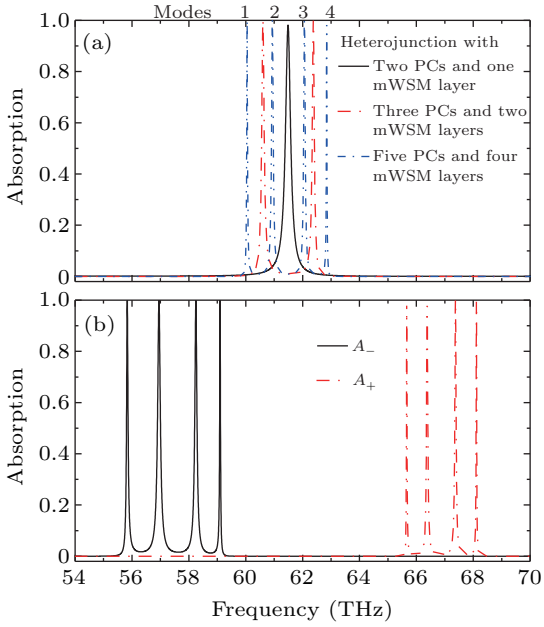


Fig. 3. The tetra-band spin-dependent PA induced by TES coupled mode. Panel (a) shows the absorption spectra of the structures PC1/mWSM/PC2, PC1/mWSM/PC2/mWSM/PC3, and PC1/mWSM/PC2/mWSM/PC3/mWSM/PC4/mWSM/PC5, where the off-diagonal term γ is hypothetically ignored. Panel (b) displays the tetra-band spin-dependent PA phenomenon for LCP and RCP light.

Based on the above discussion, the TES mode can be excited in the frequency range from 51.7 THz to 70.6 THz. To first demonstrate that TES coupled mode induces four absorption peaks of linear polarization, Fig. 3(a) shows the absorption spectra of the heterostructures with two PCs and one mWSM layer, three PCs and two mWSM layers, and five PCs and four mWSM layers. The Weyl nodes separation, Fermi energy, topological charge, and tilt degree of Weyl cones are chosen as 0.12 nm^{-1}, 0.5 eV, 2, and 0.4, respectively. The periods of five PCs are all optimized to 3.

It is found that for the structure PC1/mWSM/PC2, a PA peak appears at 61.5 THz within the TES bandgap, indicating that the PA phenomenon is enabled by the TES mode. For the structure PC1/mWSM/PC2/mWSM/PC3, two degenerate TES modes supported by PC1/mWSM/PC2 and PC2/mWSM/PC3 interact. The optical distance between the two mWSM layers, determined by the period of PC2, controls the strength of this interaction. Properly selecting this distance splits the original degenerate TES modes into two independent TES modes, forming two narrow absorption peaks at 60.6 THz and 62.38 THz. Finally, for the structure PC1/mWSM/PC2/mWSM/PC3/mWSM/PC4/mWSM/PC5, coupling among four degenerate TES modes in PC1/mWSM/PC2, PC2/mWSM/PC3, PC3/mWSM/PC4, and PC4/mWSM/PC5 splits them into four independent TES modes, denoted as modes 1–4, generating four narrow absorption peaks at 60.05 THz, 60.94 THz, 62.07 THz, and 62.85 THz, respectively. Thus, TES coupled mode induces the four absorption peaks of linear polarization.

Furthermore, Fig. 3(b) illustrates the absorption spectra of LCP and RCP light, showing the tetra-band spin-dependent PA phenomenon. Due to the TES coupled mode and the off-diagonal term of mWSM, PA of RCP and LCP is realized at four distinct frequencies. Specifically, TES mode 1 induces PA at 55.84 THz (LCP) and 65.66 THz (RCP); TES mode 2 at 56.95 THz (LCP) and 66.38 THz (RCP); TES mode 3 at 58.25 THz (LCP) and 67.38 THz (RCP); TES mode 4 at 59.1 THz (LCP) and 68.11 THz (RCP). In summary, the tetra-band spin-dependent PA enabled by TES coupled mode is demonstrated in our structure.

Subsequently, the adjustability of the spin-dependent PA phenomenon is discussed. The dependence of mWSM permittivity on the tilt degree of Weyl cones and Fermi energy provides feasible schemes to manipulate PA. Figure 4 shows the absorption spectra of LCP and RCP at various tilt degrees and Fermi energies. As seen in Figs. 4(a) and 4(c), increasing the tilt degree causes PA frequencies of LCP and RCP for the same TES mode to increase and decrease, respectively. This is because a larger tilt reduces the off-diagonal term γ, weakening the chiral feature of mWSM. When γ vanishes, absorption curves of LCP and RCP coincide. As seen in Figs. 4(b) and 4(d), increasing Fermi energy shifts PA frequencies of both LCP and RCP to higher values, mainly because the diagonal term ε_{xx} decreases with growing Fermi energy, requiring higher TES mode frequency to maintain phase change in the mWSM layer. The PA frequency difference between LCP and RCP slightly decreases with increasing Fermi energy due to the reduced off-diagonal term γ.

Furthermore, thanks to the dependence of mWSM permittivity on topological charge and Weyl nodes separation, the tetra-band spin-dependent PA can be tuned by altering the topological charge and Weyl nodes separation. The absorption of LCP and RCP at various topological charges and Weyl nodes separations is shown in Fig. 5 to illustrate the adjustable role of topological charge and Weyl nodes separation on the PA. It is found that the tetra-band PA of LCP and RCP can be realized at different Weyl nodes separations and topological

charges. As seen in Figs. 5(a) and 5(c), with increasing Weyl nodes separation, the PA frequency of LCP and RCP enabled by the same TES mode decreases and increases, respectively. The main reason is that as the Weyl nodes separation grows, the off-diagonal term γ increases, enhancing the chiral feature of mWSM. As shown in Figs. 5(b) and 5(d), with increasing topological charge, the PA frequency of LCP and RCP enabled by the same TES mode decreases, while the relative PA frequency difference between them slightly increases. This phenomenon is primarily caused by the fact that with increasing topological charge, both off-diagonal and diagonal terms increase, enhancing the chiral feature of mWSM and decreasing the TES mode frequency to maintain the phase change in the propagation of the mWSM layer.

Finally, the effect of the mWSM thickness and the periods of the middle three PCs on the spin-dependent PA phenomenon is investigated, as displayed in Fig. 6. Here the periods of the middle three PCs are identical, denoted as N_2. It is indicated that the tetra-band PA of LCP and RCP can be achieved at different thicknesses and periods. As seen in Figs. 6(a) and 6(c), with increasing thickness, the PA frequency of LCP and RCP enabled by the same TES mode decreases. The main reason is that as the thickness grows, the PA frequency induced by the TES mode

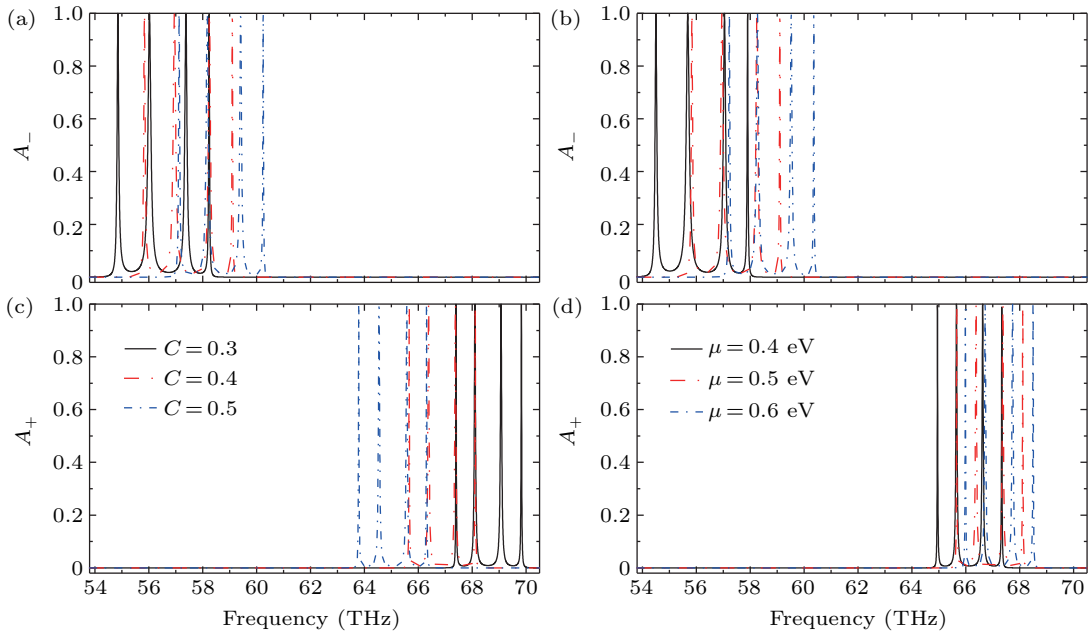


Fig. 4. Tetra-band tunable spin-dependent PA via tilt degree and Fermi energy. (a) and (c) show the absorption of LCP and RCP at different tilt degrees, respectively. (b) and (d) show the absorption of LCP and RCP at different Fermi energies, respectively.

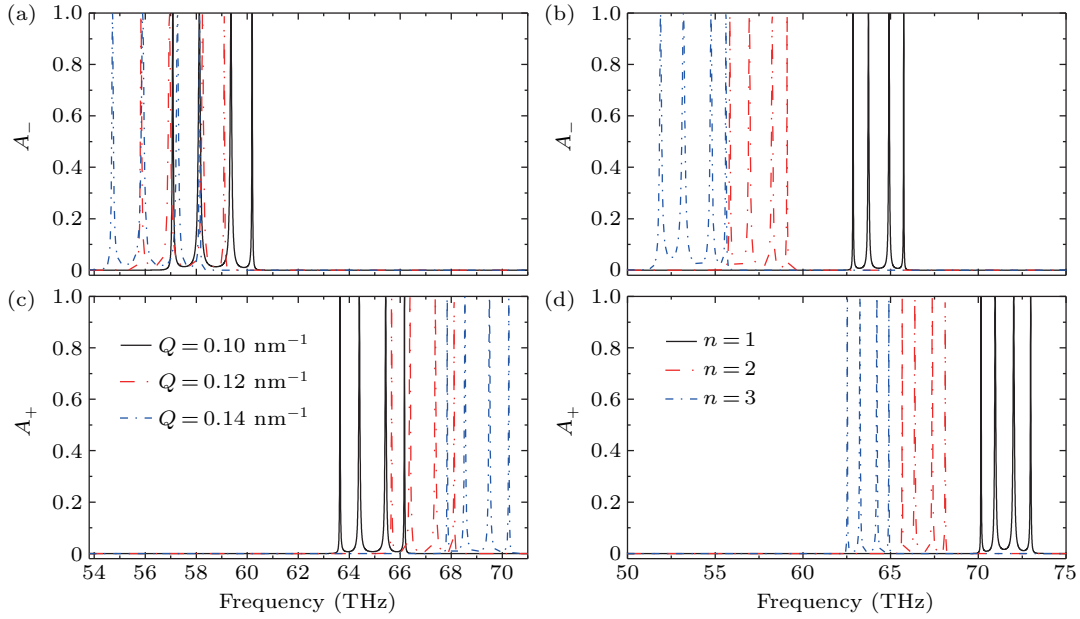


Fig. 5. Tetra-band tunable spin-dependent PA via topological charge and Weyl nodes separation. (a) and (c) show the absorption of LCP and RCP at different Weyl nodes separations, respectively. (b) and (d) show the absorption of LCP and RCP at different topological charges, respectively.

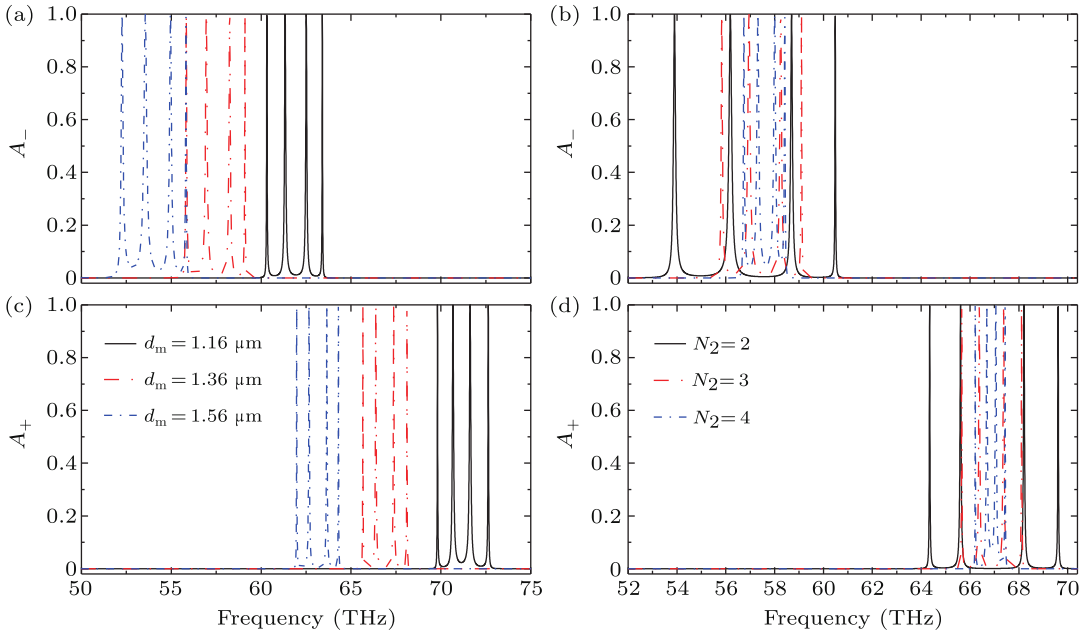


Fig. 6. Tetra-band tunable spin-dependent PA via mWSM thickness and the periods of the middle three PCs. (a) and (c) show the absorption of LCP and RCP at different mWSM thicknesses, respectively. (b) and (d) show the absorption of LCP and RCP at different periods, respectively.

must decrease to maintain the phase change in the propagation of the mWSM layer. It is found in Figs. 6(b) and 6(d) that with N_2 increasing from 2 to 4, the four PA frequencies of LCP and RCP shift toward their respective central frequencies. The main reason is that as N_2 grows, the interaction strength among the four TES modes decreases, resulting in a weakened mode-coupling splitting phenomenon.

4. Conclusion

In this article, a heterostructure containing five 1D PCs and four identical mWSM layers is developed to investigate the spin-dependent PA phenomenon by effectively combining the TES mode and the characteristics of mWSM. Results show that, due to the TES coupled mode and the chiral features supported by the off-diagonal term of mWSM, the PA of LCP and RCP is realized at four distinct frequencies, respectively, demonstrating the realization of tetra-band spin-dependent PA. Furthermore, the four PA frequencies of LCP and RCP can be flexibly regulated via the tilt degree of Weyl cones, Fermi energy, topological charge, and Weyl nodes separation. Finally, the effect of the mWSM thickness and the periods of the middle three PCs on the spin-dependent PA phenomenon is discussed. The study reveals an efficient scheme to attain tetra-band tunable spin-dependent PA without an applied magnetic field, and may provide potential applications in tunable multi-band spin-dependent photonic aspects, such as multispectral imaging and multi-channel communication.

Acknowledgments

We sincerely appreciate Dr. Jie Tang and Dr. Leyong Jiang for discussions on the innovation of this work.

This project is supported by the Education Department of Hunan Province (Grant Nos. 23B0571 and 24C0266), the Natural Science Foundation of Hunan Province (Grant No. 2023JJ40265), and the National Natural Science Foundation of China (Grant No. 12374302).

References

[1] Chang W J, Sakotic Z, Ware A, Green A M, Roman B J, Kim K, Truskett T M, Wasserman D and Milliron D J 2023 *ACS Nano* **18** 972
[2] Li Y, Huang Z Q, Xu Y F, Zhang H, Wang Q X, Qiao H X, Shang W, Deng T and Cui K H 2022 *Adv. Funct. Mater.* **32** 2207239
[3] Liu M Q, Xia S, Wan W J, Qin J, Li H, Zhao C Y, Bi L and Qiu C W 2023 *Nat. Mater.* **22** 1196
[4] Wu J P, Jiang L Y, Guo J, Dai X Y, Xiang Y J and Wen S C 2016 *Opt. Express* **24** 17103
[5] Li L, Wu Q Q, Wang C L, Cai Z Y, Lin L L, Gu X F, Ostrikov K K, Nan H Y and Xiao S Q 2024 *ACS Photonics* **11** 2615
[6] Fink Y, Winn J N, Fan S H, Chen C P, Michel J, Joannopoulos J D and Thomas E L 1998 *Science* **282** 1679
[7] Deng C S, Peng Z X and Li B X 2025 *Adv. Quantum Technol.* **8** 2400637
[8] Peng Z X, Li B X and Deng C S 2025 *Opt. Laser Technol.* **181** 111617
[9] Xu R Y, Fujikata J and Takahara J 2023 *Opt. Lett.* **48** 1490
[10] Wang X, Jiang X, You Q, Guo J, Dai X Y and Xiang Y J 2017 *Photonics Res.* **5** 536
[11] Plum E and Zheludev N I 2015 *Appl. Phys. Lett.* **106** 221901
[12] Zhou Y J, Wang Y X, Song Y H, Zhao S S, Zhang M J, Li G G, Guo Q, Tong Z, Li Z Y, Jin S, Yao H B, Zhu M Z and Zhuang T T 2024 *Nat. Commun.* **15** 251
[13] Guo Q, Li Z Y, Zhou Y J, Zhao S S, Wang Y X, Zhang M J, Li G G, Tong Z, Zhuang T T and Yu S H 2025 *Sci. Adv.* **11** eadv2721
[14] Er E, Chow T H, Liz-Marzan L M and Kotov N A 2024 *ACS Nano* **18** 12589
[15] Freiser M 1968 *IEEE Trans. Magn.* **4** 152
[16] Ju L, Geng B S, Horng J, Girit C, Martin M, Hao Z, Bechtel H A, Liang X G, Zettl A, Shen Y R and Wang F 2011 *Nat. Nanotechnol.* **6** 630
[17] Hendry E, Hale P J, Moger J, Savchenko A K and Mikhailov S A 2010 *Phys. Rev. Lett.* **105** 097401
[18] Hosur P, Parameswaran S A and Vishwanath A 2012 *Phys. Rev. Lett.* **108** 046602
[19] Xu S Y, Belopolski I, Alidoust N, *et al.* 2015 *Science* **349** 613

[20] Lv B Q, Weng H M, Fu B B, Wang X P, Miao H, Ma J, Richard P, Huang X C, Zhao L X, Chen G F, Fang Z, Dai X, Qian T and Ding H 2015 *Phys. Rev. X* **5** 031013

[21] Lv B Q, Xu N, Weng H M, Ma J Z, Richard P, Huang X C, Zhao L X, Chen G F, Matt C E, Bisti F, Strocov V N, Mesot J, Fang Z, Dai X, Qian T, Shi M and Ding H 2015 *Nat. Phys.* **11** 724

[22] Ghosh S, Sahoo A and Nandy S 2023 *SciPost Phys.* **15** 133

[23] Fang C, Gilbert M J, Dai X and Bernevig B A 2012 *Phys. Rev. Lett.* **108** 266802

[24] Huang S M, Xu X Y, Belopolski I, Lee C C, Chang G, Chang T R, Wang B K, Alidoust N, Bian G, Neupane M, Sanchez D, Zheng H, Jeng H T, Bansil A, Neupert T, Lin H and Hasan M Z 2016 *Proc. Natl. Acad. Sci. USA* **113** 1180

[25] Liu Q H and Zunger A 2017 *Phys. Rev. X* **7** 021019

[26] Yang C Y, Zhao B, Cai W S and Zhang Z M 2022 *Opt. Express* **30** 3035

[27] Wu J P, Jiang L Y, Dai X Y and Xiang Y J 2022 *Phys. Rev. A* **105** 043519

[28] Sonowal K, Singh A and Agarwal A 2019 *Phys. Rev. B* **100** 085436

[29] Asadchy V S, Guo C, Zhao B and Fan S H 2020 *Adv. Opt. Mater.* **8** 2000100

[30] Wang Y F, Khandekar C, Gao X Y, Li T C, Jiao D and Jacob Z 2021 *Opt. Mater. Express* **11** 3880

[31] Wu J P, Zeng R Z, Liang J J, Huang D, Dai X Y and Xiang Y J 2023 *Opt. Express* **31** 30079

[32] Ma W Y, Cui X, Qian L M, Ye J F, Xian F L and Zheng G G 2024 *Phys. Scripta* **100** 015516

[33] Chen W Q, Gou Y, Zhang J W, Niu T M, Ma Q, Ma H F, Mei Z L and Cui T J 2023 *Adv. Opt. Mater.* **11** 2300304

[34] Sreekanth K V, ElKabbash M, Alapan Y, Rashed A R, Gurkan U A and Strangi G 2016 *Sci. Rep.* **6** 26272

[35] Rechtsman M C, Zeuner J M, Plotnik Y, Lumer Y, Podolsky D, Dreisow F, Nolte S, Segev M and Szameit A 2013 *Nature* **496** 196

[36] Lu L, Joannopoulos J D and Soljačić M 2014 *Nat. Photonics* **8** 821

[37] Xiao M, Ma G C, Yang Z Y, Sheng P, Zhang Z Q and Chan C T 2015 *Nat. Phys.* **11** 240

[38] Wu L H and Hu X 2024 *Phys. Rev. Lett.* **114** 223901

[39] Lu L, Fang C, Fu L, Johnson S G, Joannopoulos J D and Soljacic M 2016 *Nat. Phys.* **12** 337

[40] Long X, Bao Y W, Yuan H X, Zhang H Y, Dai X Y, Li Z F, Jiang L Y and Xiang Y J 2022 *Opt. Express* **30** 20847

[41] Xu J, Fu X M, Peng Y X, Wang S P, Zheng Z W, Zou X, Qian S Y and Jiang L Y 2021 *Opt. Express* **29** 30348

[42] Luo M, Pu X T and Xiao Y 2024 *Int. J. Heat Mass Transfer.* **218** 124816

[43] Choi K H, Ling C W, Lee K F, Tsang Y H and Fung K H 2016 *Opt. Lett.* **41** 1644

[44] Liang Y Z, Xiang Y J and Dai X Y 2020 *Opt. Express* **28** 24560